

Article

# Design of High-Power Red VCSEL on a Removable Substrate

Chun-Yen Peng <sup>1</sup>, Wei-Ta Huang <sup>1,2</sup>, Zhi-Kuang Lu <sup>2</sup>, Shih-Chen Chen <sup>1</sup> and Hao-Chung Kuo <sup>1,2,\*</sup><sup>1</sup> Semiconductor Research Center, Hon Hai Research Institute, Taipei 11492, Taiwan<sup>2</sup> Department of Photonics, College of Electrical and Computer Engineering, National Yang Ming Chiao Tung University, Hsinchu 30010, Taiwan

\* Correspondence: hckuo0206@nycu.edu.tw

**Abstract:** In this work, the architecture of a high-power InAlGaP/InGaP vertical-cavity surface-emitting laser (VCSEL) with an emission wavelength of 680 nm was studied. The design of quantum well, including the well thickness, indium composition, and barrier aluminum composition targeting the emission wavelength, was elaborately optimized. Moreover, the influences of leakage current, temperature dependence of optical gain, and resonance mode gain to threshold current under different barrier aluminum compositions were investigated. Lastly, the temperature characteristics of InAlGaP/InGaP VCSEL with substrate removal have also been calculated with 24% and 40.6% improvement in thermal resistance and operating current range, respectively. It holds great promise for high-power red VCSEL application.

**Keywords:** vertical-cavity surface-emitting laser; leakage effect; quantum well; strain; material gain; substrate removal

## 1. Introduction

Since light detection and ranging (LiDAR) technologies are booming on cell phones and self-driving systems in recent years, the development of semiconductor lasers has attracted much attention. In fact, in addition to the application of LiDAR, semiconductor lasers have been widely used in consumer and professional applications that include optical disk recording [1,2], sensor applications [3,4], optical communication [5], laser display [6], pointer technology [7], and solid-state laser pumping [8]. The history of semiconductor lasers can be traced back at least 60 years ago. The first semiconductor diode laser was born in 1962 by Hall et al. [9] with an infrared (IR) wavelength and by Holonyak and Bevacqua [10] with a visible (red) wavelength. The laser cavities fabricated by homogeneous junction were parallel to the crystal surface, which are known as “edge-emitting” lasers (EEL). Although edge-emitting laser structures can confine photons in resonant cavities, laser structures with homogeneous junctions lack refractive index and energy band differences, resulting in a feeble carrier and optical confinement. In 1963, Herbert Kroemer and Zhores I. Alferov suggested adding a layer with different compositions and bandgap to create a heterojunction that would trap electrons at the junction more efficiently [11]. The heterojunction invention facilitates the operation of diode lasers at room temperature [12,13] and serves as a cornerstone for the development of quantization. The first quantum wells (QWs) were added in the active regions of semiconductor diode laser in 1978 [14,15]. Quantum well technology is an important achievement, enabling most of today’s high-efficiency LEDs and semiconductor lasers.

In fact, EELs have several disadvantages that make the manufacturing cost prohibitive, such as elliptical spots, catastrophic optical damage (COD) of facets, and testing limitations. Auspiciously, these shortcomings can be solved by “surface-emitting” lasers (SEL). The first p-n junction-based electrically-pumped SEL is proposed by the Iga group from the Tokyo Institute of Technology in 1979 [16]. In the absence of current and optical confinement, the threshold current of the first SEL is as high as 44 kA/cm<sup>2</sup> under pulse current injection



**Citation:** Peng, C.-Y.; Huang, W.-T.; Lu, Z.-K.; Chen, S.-C.; Kuo, H.-C. Design of High-Power Red VCSEL on a Removable Substrate. *Photonics* **2022**, *9*, 763. <https://doi.org/10.3390/photonics9100763>

Received: 31 August 2022

Accepted: 8 October 2022

Published: 12 October 2022

**Publisher’s Note:** MDPI stays neutral with regard to jurisdictional claims in published maps and institutional affiliations.



**Copyright:** © 2022 by the authors. Licensee MDPI, Basel, Switzerland. This article is an open access article distributed under the terms and conditions of the Creative Commons Attribution (CC BY) license (<https://creativecommons.org/licenses/by/4.0/>).

at 77 K. To reduce the SEL threshold current, the distribution Bragg reflector (DBR) and oxide confinement layer were employed on the SEL by Deppe in 1994 [17]. This work firstly demonstrated that the oxidation process for controlling the oxide aperture to form a small volume of an optical cavity in SEL is possible. Based on the idea, the first commercial oxide-confined vertical-cavity surface-emitting laser (VCSEL) with an 850 nm emission wavelength was realized in 1997, which can operate over the temperature range from  $-80\text{ }^{\circ}\text{C}$  to  $180\text{ }^{\circ}\text{C}$  [18].

Although oxide VCSEL has achieved remarkable results in the 800 to 980 nm emission wavelength, there are still some hindrances in the 600 to 700 nm range. The hindrances come from the material limitations of the composition of QWs and DBR. Several shortcomings for these shorter wavelength VCSELs exist: (1) a small conduction band offset resulting in the electron carrier leaks from the n-type layer to the p-type layer. The leakage effect will be activated at high temperatures. This drawback restricts the maximum operating temperature and the peak optical power of these shorter wavelength VCSELs. Refs. [19–21] (2) The spontaneous ordering of aluminum gallium indium phosphide (AlGaInP) epitaxial layers grown on GaAs substrates leads to a low bandgap and micro-grain boundaries [22]. Therefore, a misorientation AlGaInP grown on (100) GaAs towards [011] direction with a disordered structure was regarded as a fabrication method with better performance QWs. Refs. [23,24] (3) To ensure that the DBR compositions as a VCSEL mirror are optical transparency, the aluminum composition in AlGaAs material is greater than 0.4 to 0.5. A short usable range of DBR compositions reduces the refractive index difference. Hence, more pair numbers of DBRs to reach the same reflectivity is not avoided. Meanwhile, when the proportion of Al in AlGaAs is close to 50%, the thermal conductivity and electrical conductivity are the lowest [25–27]. More pair numbers of DBRs result in VCSELs with high series resistance and thermal resistance, causing a rapid rise in VCSEL junction temperature [28,29]. Additionally, due to the substrate absorption, the bottom emission VCSEL is also impracticable. Summing up the various factors mentioned above, it can be found that the biggest enemies of red VCSELs are thermal effects and QWs performance. Furthermore, as the operating wavelengths get shorter and shorter, these enemies will become more difficult to deal with. To quantify the effect of temperature on red light VCSELs, we used a 980 nm VCSEL with a  $5\text{ }\mu\text{m}$ -aperture [30] and a 693 nm VCSEL with a  $12\text{ }\mu\text{m}$ -aperture [31] as a cross-reference. When the ambient temperature rises from  $25\text{ }^{\circ}\text{C}$  to  $85\text{ }^{\circ}\text{C}$ , the optical power of 980 nm VCSEL decreases from 8.5 to 5.5 mW (35% decrease). In contrast, the optical power of 693 nm VCSEL drops from 7.5 to 1.5 mW (80% decrease). Under similar temperature difference conditions, the large-aperture red laser produces more severe light intensity attenuation. Therefore, if the thermal resistance of red VCSELs or the confinement effect of the quantum well can be improved, a better red VCSEL can be obtained.

So far, the development of the red VCSEL has been around 30 years since the first red VCSEL [32,33]. Most of the obstacles already have solutions. Firstly, the strained QWs to reduce the threshold current are prevalently employed on the longer wavelength (660 to 700 nm) [34–38] or the shorter wavelength (<635 nm) ranges [39–41]. The strain engineer is helpful for wavelength extension beyond that accessible from lattice-matched materials and reduces the transparency current densities [42–45]. Nevertheless, the thickness of strained QWs is limited to the critical thickness. When the total thickness of strained QWs closes the critical thickness, the dislocation defects will increase drastically. A strain-compensated QW is an effective solution [46–49]. An anti-strained direction (tensile and compressive) leads to a reduction in the strain energy and strain-misfit dislocation density, improving a red laser performance. Secondly, since the leakage current magnitude depends on the QW structures, the QW design becomes critically important. A heavily p-doped spacer layer and a high-aluminum-composition AlGaInP increasing barrier height is an intuitive method on the red laser [20,50,51]. But the maximum doping level has limitations, a high-aluminum-composition AlGaInP will hinder the impurity doping process and reduce the concentration of electron holes. Therefore, an optimal number of QW is indispensable [52–54]. Finally, a

low resistance DBR is a critical component for VCSELs in different wavelengths. A graded or abrupt doping profile with carbon as a p-doped source is helpful for a DBR with low free-carrier absorption and low resistance characteristic at the same time [55]. The detuning gain peak to the cavity wavelength is also an important design key for red VCSELs emitted at a specific temperature [21]. Different aspects of research provide a firm foundation for contemporary red VCSELs.

Nowadays, due to the rise of wearable displays and automotive head-up displays, the high-temperature characteristics of red VCSELs have attracted attention again. When red VCSELs work in outdoor environments, the obstacles mentioned previously will become more serious. To manufacture a proper VCSEL for the high-temperature environment, the design of epitaxy structures remains an important topic. However, a complete flow of the epitaxial design is rarely discussed in the past research literature. Therefore, the design flow chart of VCSEL epitaxial structures will be presented first in this report. The key to epitaxy design and experimental results in previous reports are summarized as a reference. Subsequently, Section 3 shows the design details and temperature effects of the VCSEL. Through the QW design, a VCSEL operated at a high-temperature environment can be realized. Besides epitaxial structure designs, the flip-chip process is a practical solution to reduce thermal resistance. Hence, the substrate removed VCSEL will be discussed at the end of this report. In order to improve the feasibility of red VCSEL in the outdoor application, this report will provide a complete design strategy and simulation results (performed by Crosslight PICS3D).

## 2. Design Flow

Figure 1 shows the design flow chart of a VCSEL. In designing the emission wavelength of a vertical-cavity surface-emitting laser, the bandgap of the intrinsic material is the dominant factor. However, the influence of the quantum well and strain should also be taken into account [56]. The major material systems are GaInN, AlGaInP, AlGaAs, for emission wavelength approximately around 400, 670, 800 nm, respectively [31,57–59]. For the InAlGaP/InGaP material system, the direct band gap can be expressed as [60]:

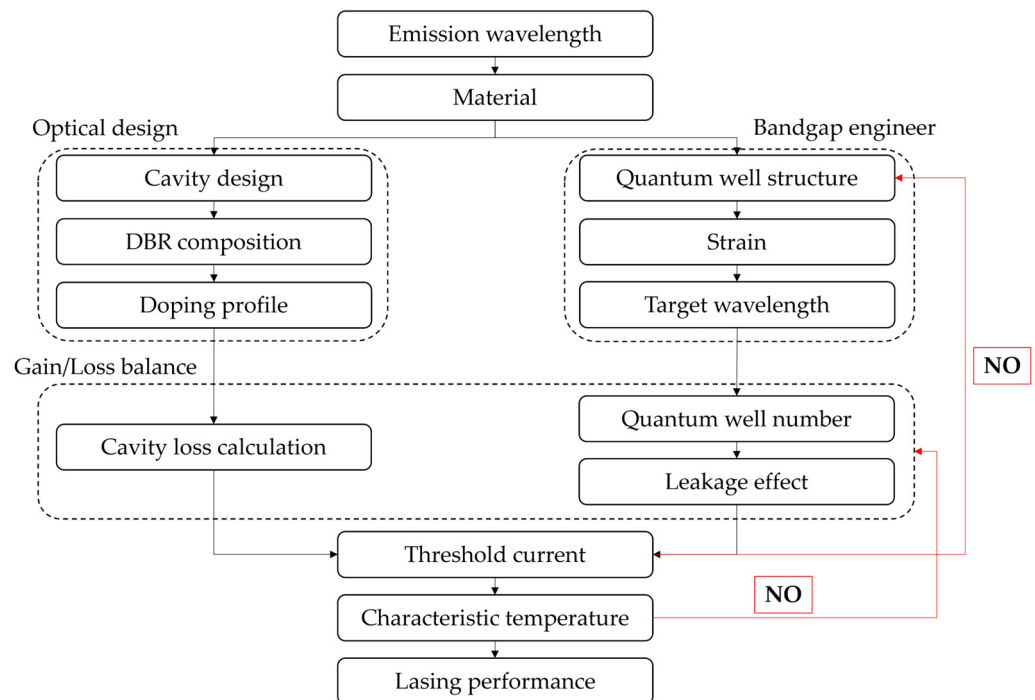


Figure 1. Design flow chart of a VCSEL.

$$E_g(In_xGa_{1-x}P) = 1.35 + 0.643(1 - x) + 0.786(1 - x)^2 \tag{1}$$

$$E_g(In_xAl_{1-x}P) = 1.35 + 1.83(1 - x) + 0.38(1 - x)^2 \tag{2}$$

$$E_g(In_x(Al_yGa_{1-y})_{1-x}P) = y \cdot E_g(InAlP) + (1 - y) \cdot E_g(InGaP) \tag{3}$$

As high-accuracy epitaxial growth techniques advanced, leading to the consistent deposition of films with accurately controlled thicknesses in the sub-nanometer range, the fabrication of heterostructures with beneficial electrical and optical characteristics became possible. The number of the supported energy level can be derived from the Schrödinger equation, where the sub-band number can be calculated from [61]:

$$n_{max} = 1 + \text{int} \left[ \sqrt{\frac{2m^*E_w t^2}{q\pi^2\hbar^2}} \right] \tag{4}$$

where  $t, E_w, m^*$  are the thickness of the quantum well, the energy difference between the well and the barrier and the effective mass, respectively. The function  $\text{int}[x]$  gives the integer part of the result.

The energy of the sub bands  $E_i$  can be derived from [62]:

$$2\sqrt{(E_w - E_i)E_i} = (2E_i - E_w)\tan\left(\sqrt{\frac{2mE_it^2}{\hbar^2}}\right), \text{ for } i = 1, 2, 3, \tag{5}$$

From the Equation (5), we can obtain the quantum confined transition energy [56]:

$$E_{QW} = \frac{\pi^2\hbar^2}{2t^2} \left( \frac{1}{m^*_v} + \frac{1}{m^*_c} \right) \tag{6}$$

Since the transition energy is correlated with the thickness of the quantum well, by adjusting it we can fine-tune the emission wavelength of the laser.

To understand the effect of strain on emission wavelength, we must first know the lattice constants of the InAlGaP/InGaP material system which are:

$$a(In_xGa_{1-x}P) = x \cdot a(InP) + (1 - x) \cdot a(GaP) \tag{7}$$

$$a(In_xAl_{1-x}P) = x \cdot a(InP) + (1 - x) \cdot a(AlP) \tag{8}$$

$$a(In_xAl_yGa_{1-y}P) = y \cdot a(InAlP) + (1 - y) \cdot a(InGaP) \tag{9}$$

By introducing tensile strain into the system, it increases the lattice constant and, consequently, decreases the energy gap. For the strain value  $\epsilon$ , hydrostatic strain  $H$  and shear strain  $S$  can be derived from:

$$\epsilon = \frac{a_{QW} - a_{barrier}}{a_{QW}} \tag{10}$$

$$H(eV) = -2a \frac{C_{11} - C_{12}}{C_{11}} \epsilon \tag{11}$$

$$S(eV) = -b \frac{C_{11} + C_{12}}{C_{11}} \epsilon \tag{12}$$

Here  $a_{QW}$  and  $a_{barrier}$  are the lattice constants of the quantum well and the barrier, respectively. With  $C_{11}$  and  $C_{12}$  as elastic stiffness coefficients,  $a$  and  $b$  as the lattice deformation potentials. The energy change due to strain is the sum of hydrostatic strain  $H$  and shear strain  $S$ , and the photon energy  $E_{hv}$  is:

$$E_{hv} = E_{g(bulk)} + E_{g(QW)} + E_{g(strain)} \tag{13}$$

After series of bandgap engineering, if the resultant emission wavelength is not desired, one may return to the beginning. Otherwise, we can discuss the gain/loss balance of the laser, that is, the quantum well number and the leakage effect.

The local gain due to a transition from a conduction band labeled  $j$  to a valence band labeled  $i$  for both the bulk and quantum well can be generally derived from [63]:

$$g_{ij}(E_{ij}^0) = \left(\frac{2\pi}{\hbar}\right) |H_{ij}|^2 (f_j' - f_i') \left(\frac{\epsilon_1}{\bar{n}c}\right) \rho_{ij} \tag{14}$$

where  $E_{ij}^0$  is the energy minimums difference between the  $i$ th valence band sub band levels and the  $j$ th conduction band sub band levels,  $H_{ij}$  is the Hamiltonian matrix element between the  $i$ th and the  $j$ th states,  $f_i'$  and  $f_j'$  are the integrated Fermi functions,  $\epsilon_1$  is the real part of the complex optical dielectric constant,  $\bar{n}$  is the real part of refractive index, and  $\rho_{ij}$  is the reduced density of states. In the case of quantum wells, many sub bands in both the valence band and the conduction band need to be considered, and the gain function is the sum of  $g_{ij}$  over all the sub bands for the allowed transitions. Furthermore, the effect of gain broaden can be take into account via the Landsberg's model, in which the quantum well form was derived by Zielinski et al. [64,65]. As the number of the quantum well increases, the confinement factor also increases; hence, larger material gain as well as the threshold current [66]. Therefore, it is important to balance between the material gain and threshold current.

In the case of valence band mixing, the gain spectrum can be obtained in numerical integration over wave number  $k_t$  [67]:

$$g(E) = \frac{g_0}{2\pi t E} \sum_{i,j} \int_0^\infty \frac{(\pi/\Gamma) f_{dip}(k_t) M_b (f_j - f_i) dk_t^2}{1 + [E_{cj}(k_t) - E_{kpi}(k_t) - E]^2/\Gamma^2} \tag{15}$$

where  $\Gamma = \hbar/\tau_{scat}$  is broadening due to intra-band scattering relaxation time  $\tau_{scat}$ ;  $f_{dip}$  is the dipole factor;  $E_{cj}$  is the  $j$ th conduction sub-band;  $E_{kpi}$  is the  $i$ th valence sub-band from the  $k \cdot p$  calculation; the sum is over all possible valence and conduction sub-bands;  $g_0$  is a constant defined as

$$g_0 = \frac{\pi q^2 \hbar}{\epsilon_0 c m_0^2 \bar{n}} \tag{16}$$

$M_b$  is the bulk dipole momentum given by:

$$M_b = \frac{1}{6} \frac{m_0 q}{m_c} \frac{E_{g0} (E_{g0} + \Delta_{so})}{E_{g0} + (2/3)\Delta_{so}} \tag{17}$$

where  $E_{g0}$  is the unstrained bandgap;  $m_c$  is the effective mass of the conduction band;  $\Delta_{so}$  is the spin-orbit coupling energy.

Moreover, the high electron mobility drifting in the cladding of an InAlGaP laser result in high leakage current, leading to higher thresholds current and a lower characteristic temperature [20]. The influence of temperature dependent threshold current has been investigated and shown that by increasing the hole concentration in the p-cladding can decrease the electron leakage current, consequently mitigate the impact toward threshold current and characteristic temperature [68]. The leakage current density can be expressed as [20]:

$$J_L = q D_n n \left[ \sqrt{\frac{1}{L_n^2} + \frac{1}{4z^2} \coth} \sqrt{\frac{1}{L_n^2} + \frac{1}{4z^2} x_p + \frac{1}{2z}} \right] \tag{18}$$

Here,  $x_p$  is the thickness of the p-cladding,  $L_n$  is the length of the minority electron diffusion,  $D_n$  is the minority electron diffusion coefficient,  $n$  is the concentration of the minority electron of p-cladding layer edge, and  $z$  is the characteristic length of the drift leakage current. Since the characteristic temperature is correlated to the quantum well

number and the leakage effect, hence, if the characteristic temperature is not desired, one may return to the gain/loss balance procedure.

Last, is the threshold current and output optical power of the laser. By taking into account the above discussion, the threshold current can be evaluated from [69]:

$$I_{th} = qn_w t B_{eff} N_i^2 \pi r^2 \left\{ \frac{2}{\alpha n_w t} \left[ a_{in} L + \log\left(\frac{1}{R}\right) \right] \right\} \quad (19)$$

where  $n_w$  is the number of the quantum wells,  $a_{in}$  is the total internal loss,  $L$  is the effective cavity length,  $R$  is the reflectivity,  $B_{eff}$  is the effective recombination constant,  $N_i$  is the carrier concentration at transparency, and  $r$  the radius of the laser. The experience equation of the output optical power can be calculated from [69]:

$$P = \frac{h\nu}{q} (I - I_{th}) \eta_d \left( 1 - \frac{\Delta T}{T_{off}} \right) \quad (20)$$

where  $\eta_d$  is the differential quantum efficiency and can be obtained from:

$$\eta_d = \eta_i \frac{\log(1/R)}{a_{in} L + \log(1/R)} \quad (21)$$

and

$$\Delta T = \frac{(V_0 + IR_d)I - P}{4\lambda_c r} \quad (22)$$

Here,  $T_{off}$  is the cutoff temperature,  $R_d$  is the series resistance,  $V_0$  is the turn-on voltage,  $\lambda_c$  is the thermal conductivity and  $\eta_i$  is the internal quantum efficiency. If the resultant laser performance is not desired, one may return to the beginning of bandgap engineering.

### 3. In AlGaP/InGaP VCSEL Structural Design and Optimization

The 680 nm VCSEL structure is shown in the Appendix A Table A1 from top to bottom. The epitaxial structure of the 680 nm VCSEL is composed by 50 pairs of Al<sub>0.45</sub>GaAs/Al<sub>0.94</sub>GaAs and five pairs of Al<sub>0.45</sub>GaAs/Al<sub>0.88</sub>GaAs n type-DBR as bottom mirror. The top mirror is a p-DBR consisting of 37 pairs of Al<sub>0.45</sub>GaAs/Al<sub>0.88</sub>GaAs. 3 pairs of InGaP/AlGaInP quantum well are sandwiched between bottom and top mirror with a 14 μm oxide aperture. The gain peak wavelength of the QW is aligned with the cavity resonant wavelength at 680 nm at room temperature. The crest of the standing wave occurs in the active region, so that the optical intensity can be effectively concentrated in the center of the active region.

First, a VCSEL with a maximum gain value at target wavelength to reach a low threshold characteristic is an expected design. Hence, the design of the VCSEL with respect to the active quantum well and the barrier was discussed at the beginning. Figure 2 shows the relationship between the well thickness and the indium composition of the well for different aluminum compositions of the barrier structure of a InGaP/AlGaInP QW emitted at 680 nm. The aluminum compositions of the barrier are 0.15, 0.25, and 0.35 for a fixed indium composition of the barrier. To fix the peak gain of QW emitted at 680 nm, the thickness of the well needs to change with the QW composition. When the indium composition of the well decreases, the bandgap of GaInP will increase. Therefore, a thick well is required to sustain the first quantum state emission at 680 nm. Likewise, the quantization effect becomes more pronounced as the barrier band gap increases, resulting in the emission wavelength emitting towards the short wavelength. Therefore, a high-aluminum barrier design will match with a thicker QW width. The relationship shown in Figure 2 can be analyzed by solving for finite QWs. The quantum number ( $v_n$ ) corresponding to each eigenvalue can be expressed:

$$v_n^2 = k_n^2 t^2 = \frac{2mt^2}{\hbar} E_n \quad (23)$$

where  $E_n$  is corresponding energy,  $t$  is the thickness of the quantum well,  $m$  is the effective mass of the carrier, and  $\hbar$  is the reduced Planck constant,  $k_n$  is dimensionless wave vector. The eigenvalue,  $v_n$ , depend on potential energy,  $V$ , which can be presented:

$$V = \frac{(E_b - E_w)}{2} \tag{24}$$

where  $E_b$  is the energy level of the barrier,  $E_w$  is the energy level of the quantum well. The indium composition of the well and the aluminum composition of the barrier correspond to  $E_w$  and  $E_b$ , respectively. If the composition of the QW changes, it will affect  $v_n$  [70]. After shifting the term, we can obtain the corresponding energy  $E_n = 2\hbar^2 v_n^2 / mt^2$ . Through the equation, the specific emission wavelength of QW structure can be decided. Moreover, by increasing the indium composition of the well, the potential energy,  $V$ , will increase resulting in a red shift wavelength. Therefore, reducing the well thickness to fix the emission wavelength at 680 nm is necessary.

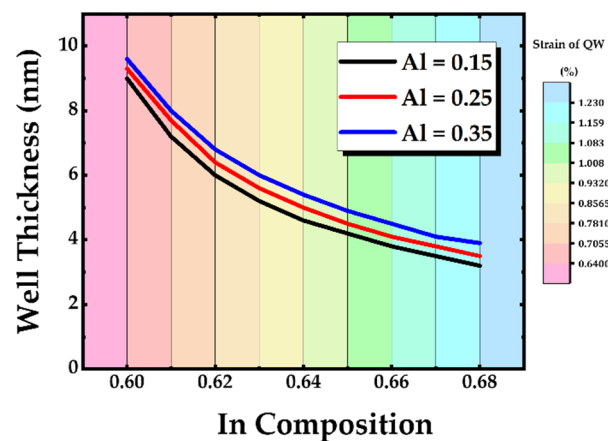


**Figure 2.** The relationship between the thickness of the well and the indium composition of the well under different barrier aluminum compositions.

Figure 2 provides viable compositions of QWs that emit at 680 nm, but it remains unclear which combination of material is the best. To understand which combination of QW compositions is the best, the simulation of maximum material gain value under different QW combinations are shown in Figure 3. The simulation shows that a high aluminum composition of the QW barrier owns a high material gain at the same indium composition of the well. The reason can be attributed to the aluminum composition of the barrier accompanied by a high energy barrier, which makes the carriers stay in the quantum well easily. On the contrary, when the aluminum composition of the barrier is reduced, a large amount of carrier spillover causes partial radiative recombination that does not contribute to the gain. This phenomenon brings about a decreased differential gain [54]. Hence, a high energy barrier for lowering the transparent current density is a favorable option. Apart from the prudent choice of the barrier height, the indium composition of the well corresponding to different quantum well widths are another major factor affecting the gain. Figure 3 shows that the change of the material gain compared to the indium composition of the well is not linear. Relative extremum can be observed at a specific indium composition of the well. Equation (14) can clearly explain this result. When the quantum well thickness is reduced, the material gain will increase due to the rise in the density of states. At the same time, the thinner well will also drop the difference of Fermi energy level between the energy level of the electron (hole), making  $(f_j - f_i)$  smaller. Therefore, when the thickness is reduced to a certain thickness, the QW will have a gain extreme value [20].

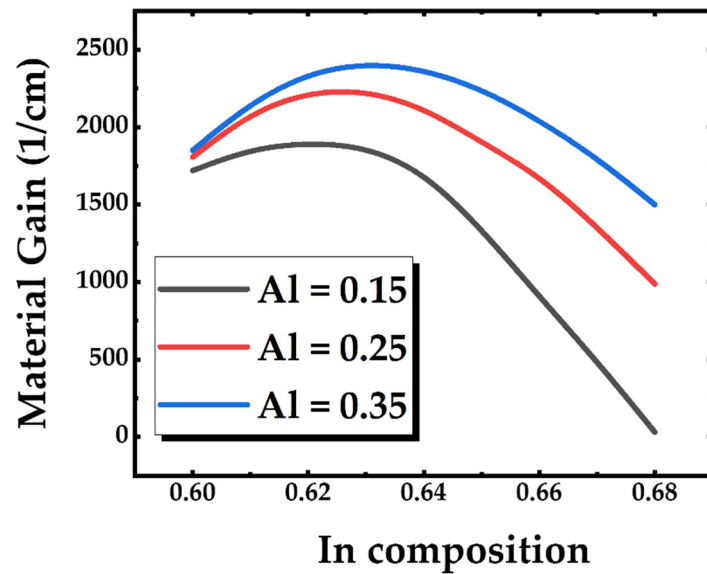


**Figure 3.** The relationship between the indium composition of well and its maximum material gain value under different barrier aluminum composition.

### 3.1. Leakage Effect

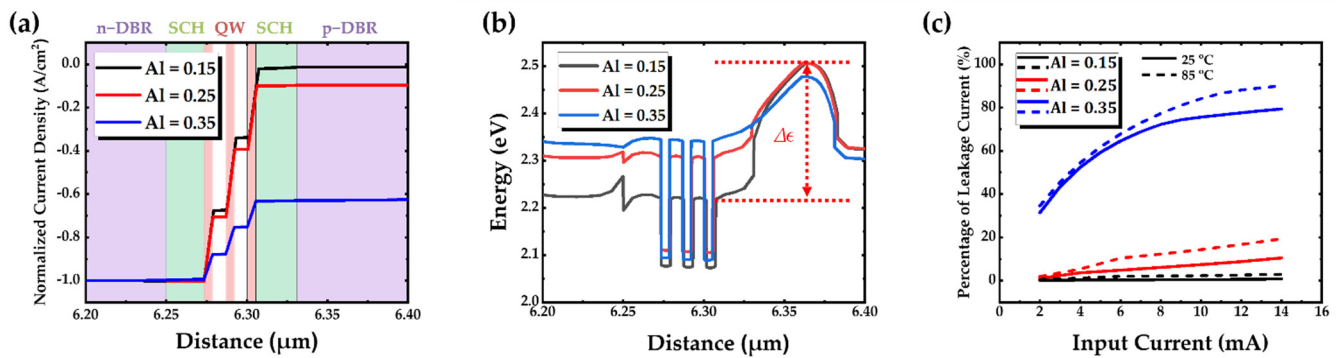
Based on the above discussion, an aluminum composition barrier with a specific indium composition of the well can provide greater gain. Larger material gain helps reduce the threshold current of the VCSEL. However, in the InAlGaP material system, the maximum aluminum content has an upper limit. The limitation comes from the junction of the direct energy gap and the indirect energy gap conversion [71] and leads to the difference in the conduction band gap becoming quite small. A small difference in the conduction band gap will decline the confinement ability of electrons and increase the susceptibility to the thermal effect, resulting in electron leaking from the n-side to the p-side more easily. In addition, a high energy barrier will narrow the energy band difference between barrier and electron confinement layer; therefore, the ability to confine the carrier will become worse, thereby enhancing the leakage current effect.

Figure 4a shows the normalized current density distribution of red VCSELs at an operating current of 10 mA at a temperature of 85 °C. The QW composition is determined from the peak point shown in Figure 3. The leakage current ratio is calculated by the normalized current density and n-DBR divides the normalized current density in p-DBR. The percentages of leakage current are 0.48%, 7.40%, and 75.58%, corresponding to the Al composition of the QW barrier of 0.15, 0.25, and 0.35, respectively. Although a higher QW barrier provides better material gain, it will exacerbate more serious leakage effects due to a smaller band gap between the barrier layer and the confinement layer is very close. The leakage current will rise sharply when the band gap between the barrier layer and the confinement layer is very close. The leakage current density can be further explored by Equation (18). In Equation (18), the minority electron concentration at the edge of the p-cladding layer,  $n$ , is expressed:

$$n = 2 \left( \frac{m_n^* kT}{2\pi\hbar^2} \right)^{\frac{3}{2}} e^{-\frac{\Delta\epsilon}{kT}} \tag{25}$$

where  $m_n^*$  is the density-of-states effective mass of electrons in the X valley of the p-confinement layer,  $\hbar$  is Planck’s constant divided by  $2\pi$ , and  $\Delta\epsilon$  is the potential barrier for electron leakage. Since the  $\Delta\epsilon$  is also equal to the energy band difference between barrier and electron confinement layer, the difference can be acquired from the conduction band diagram shown in Figure 4b. The energy band difference is 287.2, 201.6, and 113.2 meV when VCSELs are operated at 10 mA at a temperature of 85 °C, corresponding to the

Al composition of the QW barrier of 0.15, 0.25, and 0.35, respectively. After bringing energy band differences into Equation (18), the theoretical leakage current ratio is 0.18%, 5.09%, and 72.05%, respectively. The theoretical results are similar to the simulation results, providing a more reliable reference during the design flow. Furthermore, Equation (20) indicates that the temperature effect,  $T$ , and the potential barrier for electron leakage,  $\Delta\epsilon$ , on the total leakage current is an exponential function. According to the Equation (20), the leakage current will grow rapidly when the exponential function index is smaller than  $-1$ . Since leakage current is very sensitive to temperature and the potential barrier for electron leakage, designers need to carefully fine-tune the barrier height during the design flow to search an optimized QW design.



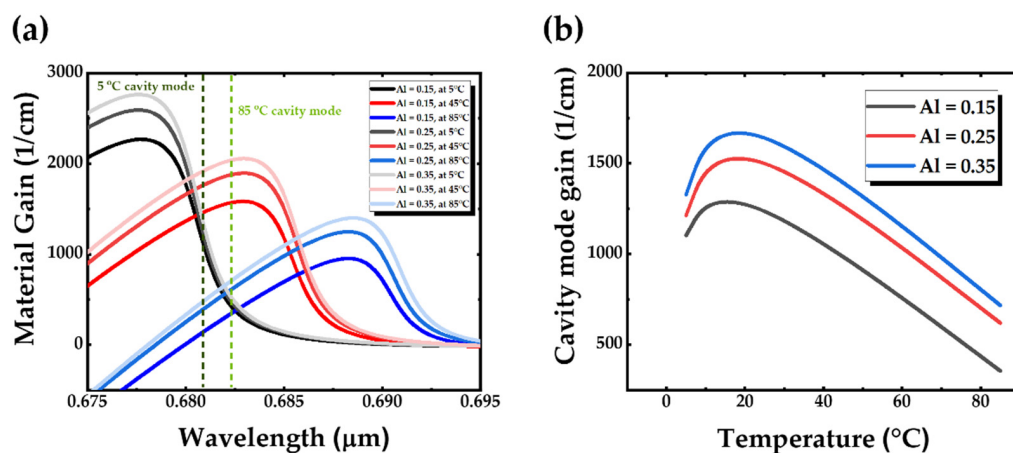
**Figure 4.** (a) Normalized current density distribution under different aluminum compositions, (b) conduction band diagram of active layer for different barrier aluminum compositions, and (c) input current density and percentage of leakage current under different aluminum compositions and temperature.

Figure 4c shows the relationship between the drive current and the percentage of leakage current under different aluminum compositions and temperatures. The simulation results show that the QW barrier with 0.15 Al composition has the best current confinement capability no matter which current is used to drive the VCSEL. The reasons have been discussed in the previous paragraphs. However, it is worth noting that the percentage of leakage current tends to increase with increasing current, regardless of the aluminum composition of the QW barrier. The upper limit of electron consumption in quantum wells is the main reason for this phenomenon. Interestingly, although the leakage current increases with the current for different QW designs, the slope of the leakage current changes with the current is not consistent. Among them, the QW barrier with 0.35 Al composition has a steepest rising slope. The QW barrier with 0.35 Al composition has a serious overflow effect that reduces the proportion of carrier recombination in the total current. The rapidly rising overflow effect will gradually slow down after the operating current reaches the threshold current. A flatness rising slope can be found after the operating current is greater than 8.12/4.11 mA and corresponds to the QW barrier with 0.35/0.25 Al composition, respectively. The flatness rising slope comes from the state transition of the VCSEL from spontaneous emission to stimulated emission, so that the injected carriers of VCSELs are converted into photons and the suppresses leakage effect. Moreover, higher operating temperatures stimulate more carrier leakage. Therefore, VCSELs operating at 85 °C has higher percentage of leakage current than that of VCSELs operating at 25 °C.

### 3.2. Temperature Dependence of Optical Gain and Resonance Mode Gain

Since a VCSEL cavity has a specific resonant wavelength, the relative position of the QW gain peak and the cavity resonant wavelength is closely related to the threshold current. In addition, as shown in Figure 5a, the red shift rates of DBR and material gain are also significantly different. The 0.25 aluminum composition is used as the data example. The redshift rate of material peak wavelength is 0.1507 nm/°C, while the change of the

cavity resonator wavelength with temperature is only 0.04 nm/°C. The material gain corresponding to the resonant wavelength will have a local extreme at different operating temperatures due to the difference in the red-shift rate between the two. The effect of local extrema also can be explained by Figure 5a. When VCSELs are operated at 5 °C, the cavity resonator wavelength is aligned on the right side of the peak of the material gain. However, the faster redshift rate of the material gain makes the material gain peak gradually across the cavity resonator wavelength. As the VCSEL operating temperature rises to 85 °C, the cavity resonator wavelength aligns to the left of the peak of the material gain. Hence, the local extrema of the cavity mode gain will appear at the temperature when the material gain peak and the cavity resonant wavelength align with each other. Figure 5b shows the relationship between temperature and cavity mode gain under different barrier aluminum compositions. Simulation results show that local extrema occur regardless of the QW composition conditions. In addition, the cavity mode gain is also very sensitive to changes in temperature. When the resonance mode moves away from the material gain peak, the cavity mode gain decreases rapidly. To make a VCSEL has the lowest threshold current at a specific operating temperature, a careful consideration of the gain to cavity offset is required during the VCSEL design flow.



**Figure 5.** Relationship between (a) gain spectrum and resonance mode gain at different temperatures and (b) temperature versus cavity mode gain, under different barrier aluminum compositions.

### 3.3. Threshold Current

Finally, the effects of the material gain and the leakage current reflected on the threshold current are organized in this section. Figure 6a shows the relationship between temperature and threshold current for different barrier aluminum compositions. The lowest threshold current appears on the 0.25 aluminum composition of the QW barrier. Compared with the 0.35/0.15 aluminum composition of the QW barrier, although the 0.25 aluminum composition of the QW barrier design does not provide the largest QW gain or the best carrier confinement, it can still achieve the lowest threshold current. The main reason can be explained by the relationship between current, spontaneous radiation and stimulated radiation for different barrier aluminum compositions as shown in Figure 6b. For spontaneous radiation rate, in general, it is positively correlated with the material gain. Therefore, the design of 0.35 aluminum composition should have the highest spontaneous emission rate. However, in the simulation of Figure 6b, the aluminum composition of 0.25 has the highest spontaneous emissivity, followed by 0.15, and the lowest spontaneous emissivity, 0.35. The opposite result than expected is caused by the leakage current phenomenon as shown in Figure 4c. At an operating current of 4 mA, the 49.8% leakage current wastes too many carriers, so that the current contributed to the spontaneous emission is only about 2 mA. Hence, the aluminum composition of 0.35 has the lowest spontaneous rate. If the leakage effect can be excluded from the drive current, we can still find that the aluminum composition of 0.35, which has the highest material gain, is helpful to reduce

the threshold current. This point of view can be demonstrated from the ratio of leakage current to threshold current. The percentage of leakage and threshold current for aluminum composition of 0.35, 0.25 and 0.15 are 72.21% at 8.12 mA, 3.64% at 4.27 mA, and 0.27% at 4.61 mA, respectively. In other words, when the VCSEL with 0.35 aluminum composition reaches the threshold current, it only takes 2.26 mA to excite the VCSEL. In contrast, the current of the 0.25/0.15 aluminum composition contributing to excite VCSEL are 4.11 and 4.59 mA. These results imply that a high material gain is still useful for a VCSEL with low threshold current.

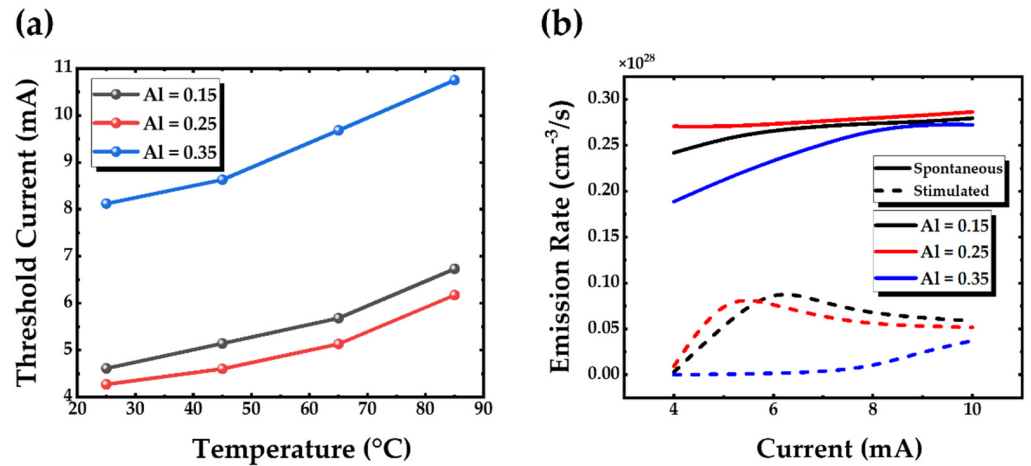


**Figure 6.** (a) Temperature versus threshold current and (b) current versus spontaneous and excited radiation rates at 25 °C, under different barrier aluminum compositions.

Moreover, by observing of the excitation radiation, the excitation radiation rates first increase rapidly with the current and then decreases gradually after VCSELs enter the excited state. The kink points occur at about 6, 5, and 10 mA when the aluminum composition is 0.15, 0.25 and 0.35, respectively. The design of the 0.15 aluminum composition QW shows the highest excitation radiation rate due to the largest energy band difference between barrier and electron confinement layer. It improves the carrier confinement ability and increases the excitation radiation rate. Furthermore, when the energy of the QW barrier increases, the depth of the quantum well also becomes deeper, leading to an uneven distribution of carriers injected into the quantum well and further affects the excited radiation rate [54]. A higher energy band difference between barrier and electron confinement layer is helpful to improve the conversion efficiency between electrons and photons of a VCSEL, thereby improving the slop efficiency of a laser. Instead, more material gain needs to be sacrificed resulting in a larger threshold current. Therefore, the optimal balance between the leakage effect and material gain needs to be achieved carefully through multiple structural revisions.

#### 4. Temperature Characteristics of InAlGaP/InGaP VCSEL with Substrates Removal

From the analysis of temperature and leakage effects, the energy band difference between barrier and electron confinement layer has an exponential relationship with the leakage current. By designing the epitaxial structure, such as the number of quantum wells and the electron blocking layer, the problem of carrier leakage can be effectively reduced. Unfortunately, it cannot reduce the thermal resistance of the VCSEL. To reduce the thermal resistance of the device, the improvement of the process structure is a more effective means. Among the different approaches, bottom-emitting VCSELs with flip-chip packaging and frontside-emitting VCSELs with substrate removal are the two most eye-catching process approaches. However, since the GaAs absorption wavelength contains 680 nm, therefore, 680 nm red VCSELs are not suitable for bottom-emitting processes, which makes frontside-emitting VCSEL technology that removes the substrate more important. Therefore, in this

section, VCSELs with different substrate thicknesses are simulated and the relationship between thermal resistance and substrate thickness is investigated.

Figure 7a shows the temperature distribution profile of a 14 μm oxide aperture VCSEL fabricated on a GaAs substrate of 65 × 65 × 100 μm (Mesa size is 18 μm) and operated at 12 mA. The temperature distribution profile shows that the isothermal curve gradually spreads toward the substrate with the VCSEL heat source as the center. The curvature of the isothermal curve gradually changes from a spherical curve to an elliptical spherical curve. When the VCSEL heat source is gradually moved away from the bottom of the substrate, the isothermal curve is nearly parallel to the substrate. In this case, when the substrate thickness is thinned, the VCSEL thermal resistance will be linearly related to the thickness. To calculate the VCSEL thermal resistance of the VCSEL, the L-I-V characteristics of the VCSEL with different substrate thicknesses are obtained by simulation as shown in Figure 7b,c, and the relationship between the junction temperature and current of the VCSEL is shown in Figure 7d, and the power conversion efficiency is 15.8%, 15.4%, 12.6%, and 9.5%, for substrate thickness of 100, 250, 400, and 500 μm, respectively, and the trend is consistent to past research [31,72].

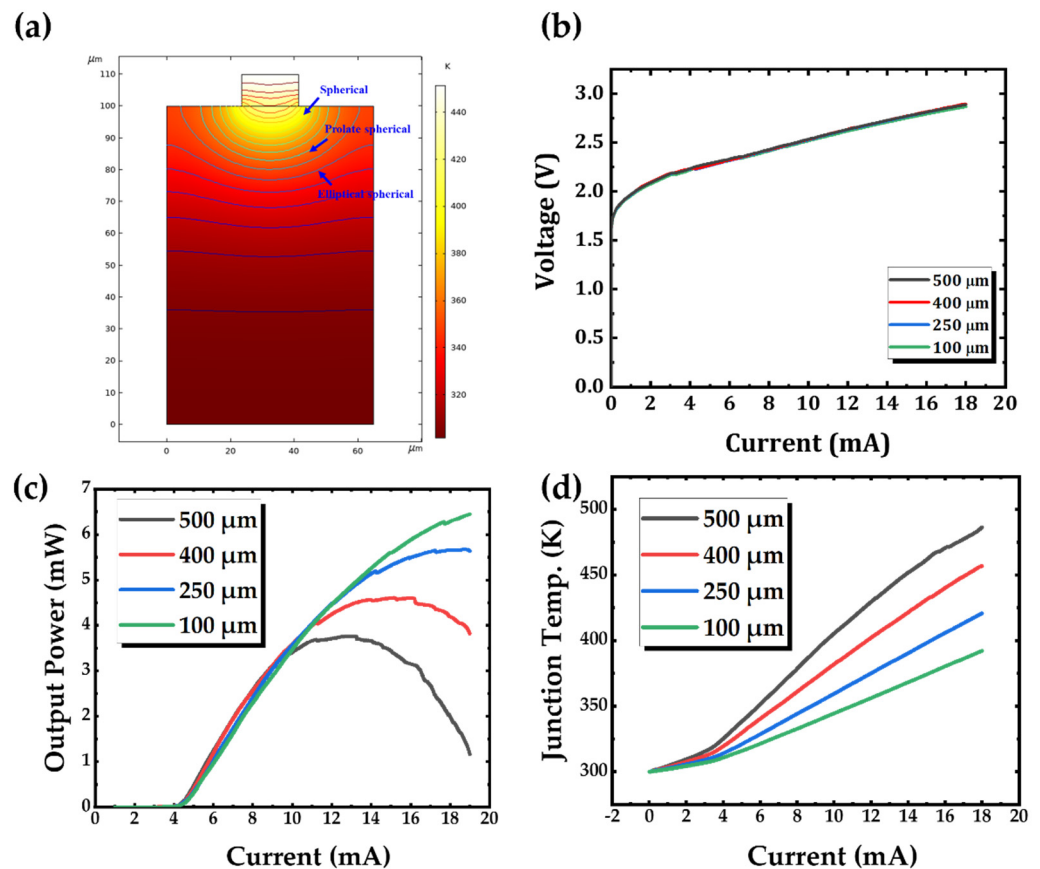


**Figure 7.** (a) Temperature distribution profile at 12 mA, (b) current-voltage relationship, (c) photoelectric characteristic curve for different substrate thicknesses, and (d) junction temperature-current relationship.

The thermal resistance can be calculated from the following Equation (26) by using the net power consumption  $P_{net}$  and the junction temperature ( $T_j$ ):

$$T_j = T_a + P_{net} \times R_{th} \tag{26}$$

where  $T_a$  and  $R_{th}$  is the environment temperature and thermal resistance of the laser, respectively, and  $P_{net} = P_{total} - P_{optical}$ . Figure 8 shows the results of laser thermal resistance calculation for different substrate thicknesses. When the thickness of VCSEL substrate

decreases from 500 to 250  $\mu\text{m}$ , the junction temperature decreases from 427 to 376 K. The thermal resistance decreases from 3936 to 2361 K/W. The result of the change of thermal resistance and thickness is a linear function. We analyze this function using the basic Equation (27) of linear thermal resistance:

$$R_{th} = R_0 + L/kA \tag{27}$$

where  $R_0$  is the intercept of the thickness of the linear function when the substrate is 0,  $L$  is the thickness of the substrate,  $k$  is the thermal conductivity of GaAs, and  $A$  is the equivalent cross-sectional area of the substrate. When the thermal conductivity of GaAs is 46, the equivalent cross-sectional area can be deduced from the slope to be  $61 \times 61 \mu\text{m}^2$ . The calculation of the equivalent area is consistent with the simulation condition. It is confirmed that when the substrate thickness is far away from the heat source, the thermal resistance and substrate thickness are a linear relationship. However, when the substrate thickness is less than 100  $\mu\text{m}$ , the linear relationship between thermal resistance and the substrate gradually deteriorates. The thermal resistance of VCSEL is 587 K/W for a substrate thickness of 0  $\mu\text{m}$ . The difference compared to the intercept  $R_0$  is 360 K/W. This difference can be explained by the distribution of the isothermal curve. As the thickness of the substrate gets closer to the VCSEL heat source, the isothermal surface is no longer parallel to the substrate cross-section. The linear thermal resistance cannot describe the lateral temperature variation, which makes the simulation results gradually deviate away from the linear function. The simulation results show that the thermal resistance can decrease from 2361 to 587 K/W resulting in a 24% difference in resistance when the VCSEL substrate thickness is significantly thinned. This result is also confirmed by the VCSEL substrate removal process in other wavelength ranges [73,74]. Furthermore, non-linear thermal resistance variations can be confirmed from the analysis of different electronic devices [72,75,76]. Therefore, the substrate thinning process is a feasible method to further improve the maximum power and operating current of red VCSELs. Figure 7b shows that the operating current increases from 12.8 to 18 mA when the thickness of the VCSEL substrate decreases from 500 to 100  $\mu\text{m}$ . The operating range is improved by 40.6% to achieve a higher power red laser. Substrate-removed VCSELs exhibit superior device performance in both high-speed VCSELs or high-power arrays. In general, substrates with a minimum thickness of 10  $\mu\text{m}$  are feasible and proven [77–80].

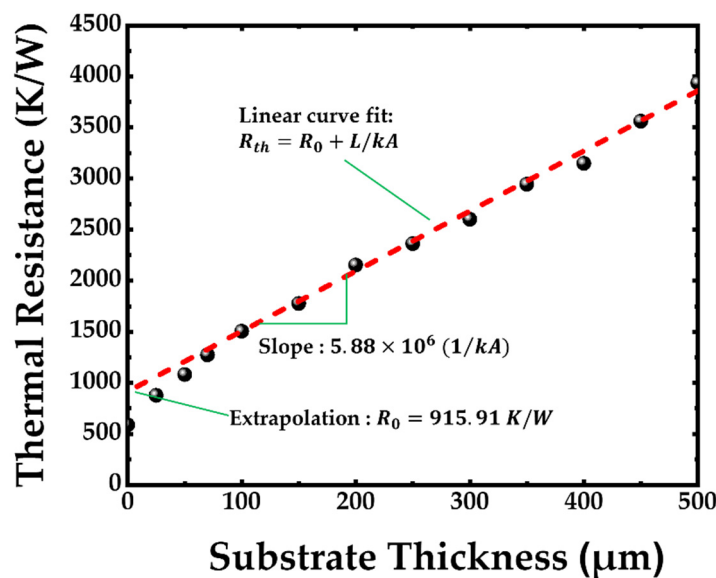


Figure 8. The thermal resistance for different substrate thicknesses.

### 5. Conclusions

In this paper, a VCSEL with an emission wavelength of 680 nm was designed by numerical simulation through design flow to improve the problem of poor heat dissipation and leakage current of the InAlGaP/InGaP material system. By fixing the target emission wavelength at 680 nm, we can obtain different combinations of indium composition corresponding to well thickness. Furthermore, the higher the aluminum composition of the barrier, the higher the energy of the barrier, making it easier for the carriers to confine in the quantum well, and hence, the lower the transparent current density, leading to higher material gain. On the other hand, when the aluminum composition of the barrier is higher, the energy difference between the confinement layer and the barrier will decrease, making the confinement of the carriers worse. When the temperature increases, the leakage effect of the carrier will be aggravated, leading to an increase in the threshold current with increasing temperature. Lastly, by substrate removal, the maximum power and operating current of VCSELs can be significantly improved, showing a promising characteristic for future high-power red VCSEL applications.

**Author Contributions:** Supervision, C.-Y.P. and H.-C.K.; writing—original draft, C.-Y.P., Z.-K.L. and W.-T.H.; Writing—Review & editing, S.-C.C. All authors have read and agreed to the published version of the manuscript.

**Funding:** This research was funded by Ministry of Science and Technology, Taiwan, grant number 110-2124-M-A49-003-, 108-2221-E-009-113-MY3.

**Institutional Review Board Statement:** Not applicable.

**Informed Consent Statement:** Not applicable.

**Data Availability Statement:** Not applicable.

**Conflicts of Interest:** The authors declare no conflict of interest.

### Appendix A

**Table A1.** The epitaxial structure of the 680 nm VCSEL.

Layer	Material	Group	Repeat	Start x	Finish x	Thickness (μm)	Dopant	Type
33	GaAs		1		N/A	0.0150	$2 \times 10^{20}$	p
32	Al <sub>x</sub> GaAs		1		0.45	0.0230	$1 \times 10^{20}$	p
31	Al <sub>x</sub> GaAs		1	0.88	0.45	0.0100	$2 \times 10^{18}$	p
30	Al <sub>x</sub> GaAs	4	37		0.88	0.0464	$3 \times 10^{18}$	p
29	Al <sub>x</sub> GaAs	4	37	0.45	0.88	0.0100	$3 \times 10^{18}$	p
28	Al <sub>x</sub> GaAs	4	37		0.45	0.0431	$3 \times 10^{18}$	p
27	Al <sub>x</sub> GaAs	4	37	0.88	0.45	0.0100	$3 \times 10^{18}$	p
26	Al <sub>x</sub> GaAs		1		0.88	0.0431	$3 \times 10^{18}$	p
25	Al <sub>x</sub> GaAs		1	0.45	0.88	0.0100	$2 \times 10^{18}$	p
24	Al <sub>x</sub> GaAs		1		0.45	0.0280	$3 \times 10^{18}$	p
23	Al <sub>x</sub> GaAs		1	0.88	0.45	0.0100	$2 \times 10^{18}$	p
22	Al <sub>x</sub> GaAs		1		0.985	0.0250	$3 \times 10^{18}$	p
21	Al <sub>x</sub> GaAs		1		0.90	0.0460	$3 \times 10^{18}$	p
20	Al <sub>x</sub> Ga <sub>1-x</sub> InP		1		0.70	0.0200	$1 \times 10^{18}$	p
19	Al <sub>x</sub> Ga <sub>1-x</sub> InP		1	0.50	0.70	0.0320	$1 \times 10^{18}$	p
18	Al <sub>x</sub> Ga <sub>1-x</sub> InP		1		0.50	0.0235	N/A	Undoped
17	InGaP		1		N/A	0.0054	N/A	Undoped
16	Al <sub>x</sub> Ga <sub>1-x</sub> InP	3	2		0.50	0.0080	N/A	Undoped
15	InGaP	3	2		N/A	0.0054	N/A	Undoped

Table A1. Cont.

Layer	Material	Group	Repeat	Start x	Finish x	Thickness ( $\mu\text{m}$ )	Dopant	Type
14	$\text{Al}_x\text{Ga}_{1-x}\text{InP}$		1		0.50	0.0235	N/A	Undoped
13	$\text{Al}_x\text{Ga}_{1-x}\text{InP}$		1	0.70	0.50	0.0500	$1 \times 10^{18}$	n
12	$\text{Al}_x\text{Ga}_{1-x}\text{InP}$		1		0.70	0.0200	$1 \times 10^{18}$	n
11	$\text{Al}_x\text{GaAs}$		1		0.88	0.0464	$2 \times 10^{18}$	n
10	$\text{Al}_x\text{GaAs}$		1	0.45	0.88	0.0100	$2 \times 10^{18}$	n
9	$\text{Al}_x\text{GaAs}$	2	5		0.45	0.0413	$2 \times 10^{18}$	n
8	$\text{Al}_x\text{GaAs}$	2	5	0.88	0.45	0.0100	$2 \times 10^{18}$	n
7	$\text{Al}_x\text{GaAs}$	2	5		0.88	0.0464	$2 \times 10^{18}$	n
6	$\text{Al}_x\text{GaAs}$	2	5	0.45	0.88	0.0100	$2 \times 10^{18}$	n
5	$\text{Al}_x\text{GaAs}$	1	50		0.45	0.0413	$2 \times 10^{18}$	n
4	$\text{Al}_x\text{GaAs}$	1	50	0.94	0.45	0.0100	$2 \times 10^{18}$	n
3	$\text{Al}_x\text{GaAs}$	1	50		0.94	0.0464	$2 \times 10^{18}$	n
2	$\text{Al}_x\text{GaAs}$	1	50	0.45	0.94	0.0100	$2 \times 10^{18}$	n
1	GaAs		1		N/A	100	$3 \times 10^{18}$	n

## References

- Goto, K. Proposal of Ultrahigh Density Optical Disk System Using a Vertical Cavity Surface Emitting Laser Array. *Jpn. J. Appl. Phys.* **1998**, *37*, 2274–2278. [\[CrossRef\]](#)
- Goto, K.; Kurihara, K. High speed VCSEL array head for tera byte optical disk. In Proceedings of the Technical Digest. CLEO/Pacific Rim '99. Pacific Rim Conference on Lasers and Electro-Optics (Cat. No.99TH8464), Online. 30 August–3 September 1999; Volume 4, pp. 1113–1114.
- Moench, H.; Carpaij, M.; Gerlach, P.; Gronenborn, S.; Gudde, R.; Hellmig, J.; Kolb, J.; van der Lee, A. *VCSEL-Based Sensors for Distance and Velocity*; SPIE: Bellingham, WA, USA, 2016; Volume 9766.
- Warren, M.; Carson, R.; Sweatt, W.; Wendt, J.; Nevers, J.; Crawford, M.; Hou, H. *VCSEL Applications in Sensors and Microsystems*; SPIE: Bellingham, WA, USA, 1998; Volume 3286.
- Liverman, S.; Bialek, H.; Natarajan, A.; Wang, A.X. VCSEL Array-Based Gigabit Free-Space Optical Femtocell Communication. *J. Lightwave Technol.* **2020**, *38*, 1659–1667. [\[CrossRef\]](#)
- Tiberi, M.; Kozlovsky, V. *Electron-Beam-Pumped VCSEL Light Source for Projection Display*; SPIE: Bellingham, WA, USA, 2005; Volume 5740.
- Iga, K. VCSEL—Its conception, development, and future. In Proceedings of the Technical Digest of the Eighteenth Microoptics Conference, Tokyo, Japan, 27–30 October 2013; pp. 1–2.
- Seurin, J.-F.; Xu, G.; Miglo, A.; Wang, Q.; Van Leeuwen, R.; Xiong, Y.; Zou, W.-X.; Li, D.; Wynn, J.; Khalfin, V.; et al. *High-Power Vertical-Cavity Surface-Emitting Lasers for Solid-State Laser Pumping*; SPIE: Bellingham, WA, USA, 2012; Volume 8276.
- Hall, R.N.; Fenner, G.E.; Kingsley, J.D.; Soltys, T.J.; Carlson, R.O. Coherent Light Emission From GaAs Junctions. *Phys. Rev. Lett.* **1962**, *9*, 366–368. [\[CrossRef\]](#)
- Holonyak, N., Jr.; Bevacqua, S.F. Coherent (visible) light emission from  $\text{Ga}(\text{As}_{1-x}\text{P}_x)$  junctions. *Appl. Phys. Lett.* **1962**, *1*, 82–83. [\[CrossRef\]](#)
- Alferov, Z.I.; Kazarinov, R. Semiconductor laser with electric pumping. Inventor's Certificate. *U.S.S.R. Patent* **1963**.
- Hayashi, I.; Panish, M.B.; Foy, P.W.; Sumski, S. Junction lasers which operate continuously at room temperature. *Appl. Phys. Lett.* **1970**, *17*, 109–111. [\[CrossRef\]](#)
- Alferov, Z.I.; Andreev, V.; Garbuzov, D.; Zhilyaev, Y.V.; Morozov, E.; Portnoi, E.; Trofim, V. Investigation of the influence of the AlAs-GaAs heterostructure parameters on the laser threshold current and the realization of continuous emission at room temperature. *Sov. Phys. Semicond.* **1971**, *4*, 1573–1575.
- Rezek, E.A.; Holonyak, N., Jr.; Vojak, B.A.; Stillman, G.E.; Rossi, J.A.; Keune, D.L.; Fairing, J.D. LPE  $\text{In}_{1-x}\text{Ga}_x\text{P}_{1-z}\text{As}_z$  ( $x \sim 0.12$ ,  $z \sim 0.26$ ) DH laser with multiple thin-layer ( $< 500 \text{ \AA}$ ) active region. *Appl. Phys. Lett.* **1977**, *31*, 288–290. [\[CrossRef\]](#)
- Holonyak, N., Jr.; Kolbas, R.M.; Dupuis, R.D.; Dapkus, P.D. Room-temperature continuous operation of photopumped MO-CVD  $\text{Al}_x\text{Ga}_{1-x}\text{As-GaAs-Al}_x\text{Ga}_{1-x}\text{As}$  quantum-well lasers. *Appl. Phys. Lett.* **1978**, *33*, 73–75. [\[CrossRef\]](#)
- Soda, H.; Iga, K.-i.; Kitahara, C.; Suematsu, Y. GaInAsP/InP Surface Emitting Injection Lasers. *Jpn. J. Appl. Phys.* **1979**, *18*, 2329–2330. [\[CrossRef\]](#)
- Huffaker, D.L.; Deppe, D.G.; Kumar, K.; Rogers, T.J. Native-oxide defined ring contact for low threshold vertical-cavity lasers. *Appl. Phys. Lett.* **1994**, *65*, 97–99. [\[CrossRef\]](#)
- Choquette, K.D.; Hou, H.Q. Vertical-cavity surface emitting lasers: Moving from research to manufacturing. *Proc. IEEE* **1997**, *85*, 1730–1739. [\[CrossRef\]](#)

19. Martin, O.J.F.; Bona, G.L.; Wolf, P. Thermal behavior of visible AlGaInP-GaInP ridge laser diodes. *IEEE J. Quantum Electron.* **1992**, *28*, 2582–2588. [[CrossRef](#)]
20. Bour, D.P.; Treat, D.W.; Thornton, R.L.; Geels, R.S.; Welch, D.F. Drift leakage current in AlGaInP quantum-well lasers. *IEEE J. Quantum Electron.* **1993**, *29*, 1337–1343. [[CrossRef](#)]
21. Knowles, G.; Sweeney, S.; Sale, T. Influence of leakage and gain-cavity alignment on the performance of Al (GaInP) visible vertical-cavity surface emitting lasers. *IEEE Proc. Optoelectron.* **2001**, *148*, 55–59. [[CrossRef](#)]
22. Gomyo, A.; Suzuki, T.; Kobayashi, K.; Kawata, S.; Hino, I.; Yuasa, T. Evidence for the existence of an ordered state in Ga<sub>0.5</sub>In<sub>0.5</sub>P grown by metalorganic vapor phase epitaxy and its relation to band-gap energy. *Appl. Phys. Lett.* **1987**, *50*, 673–675. [[CrossRef](#)]
23. Hiroyama, R.; Hamada, H.; Shono, M.; Honda, S.; Yodoshi, K.; Yamaguchi, T. 630 nm-band AlGaInP strained MQW laser diodes with an MQB grown on misoriented substrates. In Proceedings of the 13th IEEE International Semiconductor Laser Conference, Takamatsu, Japan, 21–25 September 1992; pp. 154–155.
24. Hamada, H. Characterization of Gallium Indium Phosphide and Progress of Aluminum Gallium Indium Phosphide System Quantum-Well Laser Diode. *Materials* **2017**, *10*, 875. [[CrossRef](#)] [[PubMed](#)]
25. Piprek, J.; Troger, T.; Schroter, B.; Kolodzey, J.; Ih, C.S. Thermal conductivity reduction in GaAs-AlAs distributed Bragg reflectors. *IEEE Photonics Technol. Lett.* **1998**, *10*, 81–83. [[CrossRef](#)]
26. Bhattacharya, A.; Zorn, M.; Oster, A.; Nasarek, M.; Wenzel, H.; Sebastian, J.; Weyers, M.; Tränkle, G. Optimization of MOVPE growth for 650nm-emitting VCSELs. *J. Cryst. Growth* **2000**, *221*, 663–667. [[CrossRef](#)]
27. Yao, T. Thermal properties of AlAs/GaAs superlattices. *Appl. Phys. Lett.* **1987**, *51*, 1798–1800. [[CrossRef](#)]
28. Chow, W.W.; Choquette, K.D.; Crawford, M.H.; Lear, K.L.; Hadley, G.R. Design, fabrication, and performance of infrared and visible vertical-cavity surface-emitting lasers. *IEEE J. Quantum Electron.* **1997**, *33*, 1810–1824. [[CrossRef](#)]
29. Knowles, G.; Sweeney, S.; Sale, T.; Adams, A. Self-heating effects in red (665 nm) VCSELs. *IEE Proc. Optoelectron.* **2001**, *148*, 256–260. [[CrossRef](#)]
30. Mutig, A.; Fiol, G.; Potschke, K.; Moser, P.; Arsenijevic, D.; Shchukin, V.A.; Ledentsov, N.N.; Mikhrin, S.S.; Krestnikov, I.L.; Livshits, D.A.; et al. Temperature-Dependent Small-Signal Analysis of High-Speed High-Temperature Stable 980-nm VCSELs. *IEEE J. Sel. Top. Quantum Electron.* **2009**, *15*, 679–686. [[CrossRef](#)]
31. Johnson, K.; Hibbs-Brenner, M.; Hogan, W.; Dummer, M. Advances in Red VCSEL Technology. *Adv. Opt. Technol.* **2012**, *2012*, 569379. [[CrossRef](#)]
32. Lott, J.; Schneider, R. Electrically injected visible (639–661 nm) vertical cavity surface emitting lasers. *Electron. Lett.* **1993**, *29*, 830–832. [[CrossRef](#)]
33. Huang, K.F.; Tai, K.; Wu, C.C.; Wynn, J.D. Continuous wave visible InGaP/InGaAlP quantum-well surface-emitting laser diodes. *IEEE Trans. Electron Devices* **1993**, *40*, 2119. [[CrossRef](#)]
34. Katsuyama, T.; Yoshida, I.; Shinkai, J.; Hashimoto, J.; Hayashi, H. Very low threshold current AlGaInP/Ga<sub>x</sub>In<sub>1-x</sub>P strained single quantum well visible laser diode. *Electron. Lett.* **1990**, *17*, 1375–1377. [[CrossRef](#)]
35. Serreze, H.B.; Chen, Y.C. Low-threshold, strained-layer, GaInP/AlGaInP GRINSCH visible diode lasers. *IEEE Photonics Technol. Lett.* **1991**, *3*, 397–399. [[CrossRef](#)]
36. Katsuyama, T.; Yoshida, I.; Shinkai, J.; Hashimoto, J.; Hayashi, H. High temperature ( $\geq 150$  °C) and low threshold current operation of AlGaInP/Ga<sub>x</sub>In<sub>1-x</sub>P strained multiple quantum well visible laser diodes. *Appl. Phys. Lett.* **1991**, *59*, 3351–3353. [[CrossRef](#)]
37. Mannoh, M.; Hoshina, J.; Kamiyama, S.; Ohta, H.; Ban, Y.; Ohnaka, K. High power and high-temperature operation of GaInP/AlGaInP strained multiple quantum well lasers. *Appl. Phys. Lett.* **1993**, *62*, 1173–1175. [[CrossRef](#)]
38. Blood, P.; Smowton, P. Strain dependence of threshold current in fixed-wavelength GaInP laser diodes. *IEEE J. Sel. Top. Quantum Electron.* **1995**, *1*, 707–711. [[CrossRef](#)]
39. Kobayashi, R.; Hotta, H.; Miyasaka, F.; Hara, K.; Kobayashi, K. Low-threshold, highly reliable 630 nm-band AlGaIP visible laser diodes with AlInP buried waveguide. *Electron. Lett.* **1996**, *32*, 894–896. [[CrossRef](#)]
40. Watanabe, M.; Matsuura, H.; Shimada, N.; Okuda, H. Optimum tensile-strained multiquantum-well structure of 630-nm band InGaAlP lasers for high temperature and reliable operation. *IEEE J. Sel. Top. Quantum Electron.* **1995**, *1*, 712–716. [[CrossRef](#)]
41. Tanaka, T.; Yanagisawa, H.; Kawanaka, S.; Minagawa, S. Study on strain-induced polarization mode of strained-layer quantum-well 630-nm AlGaInP LD's. *IEEE Photonics Technol. Lett.* **1995**, *7*, 136–139. [[CrossRef](#)]
42. Valster, A.; van der Poel, C.J.; Finke, M.N.; Boermans, M.J.B. Effect of strain on the threshold current of GaInP/AlGaInP quantum well lasers emitting at 633 nm. In Proceedings of the 13th IEEE International Semiconductor Laser Conference, Kagazwa, Japan, 21–25 September 1992; pp. 152–153.
43. Kamiyama, S.; Uenoyama, T.; Mannoh, M.; Ohnaka, K. Strain Effect on 630 nm GaInP/AlGaInP Multi-Quantum Well Lasers. *Jpn. J. Appl. Phys.* **1994**, *33*, 2571–2578. [[CrossRef](#)]
44. Kamiyama, S.; Monnoh, M.; Ohnaka, K.; Uenoyama, T. Studies of threshold current dependence on compressive and tensile strain of 630 nm GaInP/AlGaInP multi-quantum-well lasers. *J. Appl. Phys.* **1994**, *75*, 8201–8203. [[CrossRef](#)]
45. Smowton, P.; Summers, H.; Rees, P.; Blood, P. *Optimization of 670-nm Strained Quantum well Laser Diodes*; SPIE: Bellingham, WA, USA, 1994; Volume 2148.

46. Hiroyama, R.; Bessho, Y.; Kase, H.; Ikegami, T.; Honda, S.; Shono, M.; Yodoshi, K.; Yamaguchi, T.; Niina, T. Strain-compensated multiple quantum well 630-nm-band AlGaInP laser diodes. In Proceedings of the IEEE 14th International Semiconductor Laser Conference, Maui, HI, USA, 19–23 September 1994; pp. 205–206.
47. Valster, A.; Meney, A.T.; Downes, J.R.; Faux, D.A.; Adams, A.R.; Brouwer, A.A.; Corbijn, A.J. Strain-overcompensated GaInP-AlGaInP quantum-well laser structures for improved reliability at high-output powers. *IEEE J. Sel. Top. Quantum Electron.* **1997**, *3*, 180–187. [[CrossRef](#)]
48. Tansu, N.; Zhou, D.; Mawst, L.J. Low-temperature sensitive, compressively strained InGaAsP active ( $\lambda = 0.78\text{--}0.85\ \mu\text{m}$ ) region diode lasers. *IEEE Photonics Technol. Lett.* **2000**, *12*, 603–605. [[CrossRef](#)]
49. Yu, Y.; Zhang, X.; Huang, B.; Wang, D.; Wei, J.; Zhou, H.; Pan, J.; Qi, Y.; Chen, W.; Qin, X.; et al. Strain effect and characteristics of GaInP/AlGaInP strain-compensated multiple quantum wells. *Mater. Sci. Eng. B* **2003**, *97*, 211–216. [[CrossRef](#)]
50. Schneider, R.P., Jr.; Crawford, M.H.; Choquette, K.D.; Lear, K.L.; Kilcoyne, S.P.; Figiel, J.J. Improved AlGaInP-based red (670–690 nm) surface-emitting lasers with novel C-doped short-cavity epitaxial design. *Appl. Phys. Lett.* **1995**, *67*, 329–331. [[CrossRef](#)]
51. Ohba, Y.; Nishikawa, Y.; Nozaki, C.; Sugawara, H.; Nakanisi, T. A study of p-type doping for AlGaInP grown by low-pressure MOCVD. *J. Cryst. Growth* **1988**, *93*, 613–617. [[CrossRef](#)]
52. Huang, M.-F.; Tsai, M.-L.; Kuo, Y.-K. *Improvement of Characteristic Temperature for AlGaInP Laser Diodes*; SPIE: Bellingham, WA, USA, 2005; Volume 5628.
53. Huang, M.-F.; Sun, Y.-L. Optimization of Barrier Structure for Strain-Compensated Multiple-Quantum-Well AlGaInP Laser Diodes. *Jpn. J. Appl. Phys.* **2006**, *45*, 7600–7604. [[CrossRef](#)]
54. Huang, M.F.; Tsai, M.L.; Shin, J.Y.; Sun, Y.L.; Yang, R.M.; Kuo, Y.K. Optimization of active layer structures to minimize leakage current for an AlGaInP laser diode. *Appl. Phys. A* **2005**, *81*, 1369–1373. [[CrossRef](#)]
55. Onischenko, A.; Sale, T.; O'Reilly, E.; Adams, A.; Pinches, S.; Frost, J.; Woodhead, J. Progress in the design and development of AlGaInP visible VCSELs. *IEE Proc. Optoelectron.* **2000**, *147*, 15–21. [[CrossRef](#)]
56. Zappe, H. *Laser Diode Microsystems*; Springer Science & Business Media: Berlin, Germany, 2004.
57. Iga, K. Surface-emitting laser-its birth and generation of new optoelectronics field. *IEEE J. Sel. Top. Quantum Electron.* **2000**, *6*, 1201–1215. [[CrossRef](#)]
58. Linnik, M.; Christou, A. Group III-Nitride Based VCSEL for Applications at the Wavelength of 400nm. *MRS Online Proc. Libr.* **2001**, *639*, 642. [[CrossRef](#)]
59. Tsai, C.T.; Peng, C.Y.; Wu, C.Y.; Leong, S.F.; Kao, H.Y.; Wang, H.Y.; Chen, Y.W.; Weng, Z.K.; Chi, Y.C.; Kuo, H.C.; et al. Multi-Mode VCSEL Chip with High-Indium-Density InGaAs/AlGaAs Quantum-Well Pairs for QAM-OFDM in Multi-Mode Fiber. *IEEE J. Quantum Electron.* **2017**, *53*, 1–8. [[CrossRef](#)]
60. Casey, H.C.; Panish, M.B. *Heterostructure Lasers*; Academic Press: Cambridge, MA, USA, 1978; Volume 1.
61. Mitin, V.; Kochelap, V.; Strosio, M.A. *Quantum Heterostructures: Microelectronics and Optoelectronics*; Cambridge University Press: Cambridge, UK, 1999.
62. Merzbacher, E. *Quantum Mechanics*; Jones & Bartlett Publishers: Burlington, MA, USA, 1961.
63. Wooten, F. Optical Properties of Solids. *Am. J. Phys.* **1973**, *41*, 939–940. [[CrossRef](#)]
64. Zielinski, E.; Schweizer, H.; Hausser, S.; Stuber, R.; Pilkuhn, M.; Weimann, G. Systematics of laser operation in GaAs/AlGaAs multiquantum well heterostructures. *IEEE J. Quantum Electron.* **1987**, *23*, 969–976. [[CrossRef](#)]
65. Zielinski, E.; Keppler, F.; Hausser, S.; Pilkuhn, M.H.; Sauer, R.; Tsang, W.T. Optical gain and loss processes in GaInAs/InP MQW laser structures. *IEEE J. Quantum Electron.* **1989**, *25*, 1407–1416. [[CrossRef](#)]
66. Asada, M.; Kameyama, A.; Suematsu, Y. Gain and intervalence band absorption in quantum-well lasers. *IEEE J. Quantum Electron.* **1984**, *20*, 745–753. [[CrossRef](#)]
67. Chuang, S.L. *Physics of Photonic Devices*; John Wiley & Sons: Hoboken, NJ, USA, 2012.
68. Hagen, S.H.; Valster, A.; Boermans, M.J.B.; van der Heyden, J. Investigation of the temperature dependence of the threshold current density of GaInP/AlGaInP double-heterostructure lasers. *Appl. Phys. Lett.* **1990**, *57*, 2291–2293. [[CrossRef](#)]
69. Yu, S.F. *Analysis and Design of Vertical Cavity Surface Emitting Lasers*; John Wiley & Sons: Hoboken, NJ, USA, 2003; Volume 7.
70. Bastard, G.; Mendez, E.E.; Chang, L.L.; Esaki, L. Variational calculations on a quantum well in an electric field. *Phys. Rev. B* **1983**, *28*, 3241–3245. [[CrossRef](#)]
71. Vignaud, D.; Mollet, F. Conduction band offset in the  $\text{Al}_x\text{Ga}_{1-x}\text{In}_y\text{P}/\text{Ga}_{0.52}\text{In}_{0.48}\text{P}$  system as studied by luminescence spectroscopy. *J. Appl. Phys.* **2003**, *93*, 384–389. [[CrossRef](#)]
72. Choi, J.H.; Wang, L.; Bi, H.; Chen, R.T. Effects of Thermal-Via Structures on Thin-Film VCSELs for Fully Embedded Board-Level Optical Interconnection System. *IEEE J. Sel. Top. Quantum Electron.* **2006**, *12*, 1060–1065. [[CrossRef](#)]
73. Kuo, Y.K.; Chen, J.R.; Chen, M.L.; Liou, B.T. Numerical study on strained InGaAsP/InGaP quantum wells for 850-nm vertical-cavity surface-emitting lasers. *Appl. Phys. B* **2007**, *86*, 623–631. [[CrossRef](#)]
74. Yum, W.-S.; Lee, S.-Y.; Kim, M.-S.; Yoon, S.-J.; Oh, J.-T.; Jeong, H.-H.; Seong, T.-Y. Improving Performance of GaAs-Based Vertical-Cavity Surface-Emitting Lasers by Employing Thermally Conductive Metal Substrate. *ECS J. Solid State Sci. Technol.* **2021**, *10*, 015001. [[CrossRef](#)]
75. Chen, R.T.; Lei, L.; Chulchae, C.; Liu, Y.J.; Bihari, B.; Wu, L.; Tang, S.; Wickman, R.; Picor, B.; Hibb-Brenner, M.K.; et al. Fully embedded board-level guided-wave optoelectronic interconnects. *Proc. IEEE* **2000**, *88*, 780–793. [[CrossRef](#)]

76. Vermeersch, B.; De Mey, G. Influence of substrate thickness on thermal impedance of microelectronic structures. *Microelectron. Reliab.* **2007**, *47*, 437–443. [[CrossRef](#)]
77. Chulchae, C.; Lei, L.; Yujie, L.; Chen, R.T. Performance analysis of 10- $\mu\text{m}$ -thick VCSEL array in fully embedded board level guided-wave optoelectronic interconnects. *J. Lightwave Technol.* **2003**, *21*, 1531–1535. [[CrossRef](#)]
78. Wang, L.; Choi, J.; Wang, X.; Chen, R.; Hass, D.; Magera, J. *Thin Film Optical Waveguide and Optoelectronic Device Integration for Fully Embedded Board Level Optical Interconnects*; SPIE: Bellingham, WA, USA, 2004; Volume 5556.
79. Seurin, J.-F.; Xu, G.; Khalfin, V.; Miglo, A.; Wynn, J.; Pradhan, P.; Ghosh, C.; D'Asaro, L.A. *Progress in High-Power High-Efficiency VCSEL Arrays*; SPIE: Bellingham, WA, USA, 2009; Volume 7229.
80. Hong, K.-B.; Huang, W.-T.; Chung, H.-C.; Chang, G.-H.; Yang, D.; Lu, Z.-K.; Chen, S.-L.; Kuo, H.-C. High-Speed and High-Power 940 nm Flip-Chip VCSEL Array for LiDAR Application. *Crystals* **2021**, *11*, 1237. [[CrossRef](#)]